

Energy and linear-momentum dissipation in the fusion reaction of $^{165}\text{Ho} + ^{20}\text{Ne}$ at 30 MeV/nucleon

D. Hilscher, H. Rossner, A. Gamp,* and U. Jahnke

Hahn-Meitner-Institut Berlin, D-1000 Berlin 39, Federal Republic of Germany

B. Cheynis, B. Chambon, D. Drain, and C. Pastor

Institut de Physique Nucléaire, Université Claude Bernard Lyon, 69622 Villeurbanne, France

A. Giorni, C. Morand, A. Dauchy, and P. Stassi

Institut des Sciences Nucléaires, 38026 Grenoble, France

G. Petitt

Georgia State University, Atlanta, Georgia 30303

(Received 29 December 1986)

Neutron energy spectra were measured at angles between 14° and 159° in coincidence with evaporation residues as a function of linear-momentum transfer in reactions of ^{165}Ho with 600 MeV ^{20}Ne . In addition, angular distributions and absolute cross sections for elastic scattering, fission, and evaporation residues have been measured. The preequilibrium component of the neutron spectra has been parametrized with a hot-moving-source fit. For the highest linear-momentum transfer the forward-to-backward anisotropy in the angular distribution is smallest and the quality of the fit is best. From the temperature and multiplicity of evaporated neutrons the level density parameter of nuclei with $A \approx 180$ has been determined to be $a = A/(10.5 \pm 1) \text{ MeV}^{-1}$ at excitation energies of 300 to 400 MeV.

I. INTRODUCTION

In recent years a considerable effort was made by many groups¹⁻⁴ to study the onset and evolution of preequilibrium (PE) nucleon emission in fusion-like reactions with increasing bombarding energy. However, in order to understand the energy dissipation mechanisms it is necessary to study one system at a large range of bombarding energies. The reaction $^{20}\text{Ne} \rightarrow ^{165}\text{Ho}$ was previously studied by Holub *et al.*³ at bombarding energies of 11, 14.6, and 20.1 MeV/nucleon. These energies are smaller than the mean Fermi energy of nucleons in nuclei of 24 MeV. So it was of interest to study this system at higher bombarding energies, where one expects the transition from a mean-field approach to a nucleon-nucleon collision dominated regime. That is why we have chosen a bombarding energy of 30 MeV/nucleon.

This energy is also interesting since we can heat the fused nuclei up to temperatures of about 5 MeV and study their behavior under such extreme conditions. In particular, it is interesting to study the correlation between linear-momentum transfer and energy dissipation. This should lead to a consistent description of light-particle emission prior to and after the attainment of thermal equilibrium.

II. EXPERIMENTAL METHOD AND RESULTS

Neutrons were measured in coincidence with evaporation residues (ER's) in the reaction $^{165}\text{Ho} + ^{20}\text{Ne}$ at 600

MeV neon energy. Evaporation residues were detected at $\pm 5.3^\circ$ at a distance of 27.2 and 27.7 cm from a 500 $\mu\text{g}/\text{cm}^2$ thick metallic holmium target with two $\Delta E - \Delta E$ silicon detector telescopes. The detector aperture had a diameter of 5 mm. Both ΔE detectors were 120 μm thick. The second ΔE detector was used to reject within a few 10 ns all particles which were not stopped in the first ΔE detector, particularly all elastic and quasielastic neon ions. Using the energy of the first ΔE detector and the time of flight (TOF) as measured in reference to the beam bunches of the SARA cyclotron in Grenoble, it was possible to separate the ER's from all other fragments, as can be seen in Fig. 1.

Neutrons were detected in nine NE213 liquid scintillators with dimensions of 5 cm \times 10 cm (thickness \times diameter). These detectors enabled n- γ -pulse-shape separation, which was done off line. The neutron detectors were positioned 1.2–1.7 m from the target outside of a thin (2 mm) walled aluminum scattering chamber with a diameter of 35 cm. The detailed geometry of the detectors is shown in Fig. 2 and given in Table I. The neutron time of flight was measured in reference to fragments detected in the first ΔE detector. The correction for the heavy-ion time of flight was done off line by taking the difference between the two measured times. The total time resolution for γ -rays in coincidence with ER's was 2.5 ns full width at half maximum (FWHM). This corresponds to an energy resolution of 0.9 and 26 MeV for 8 and 80 MeV neutrons, respectively, at a path length of 1.76 m. The neutron energy spectra were averaged over the two symmetric ER angles of $\pm 5.3^\circ$ in order to remove asym-

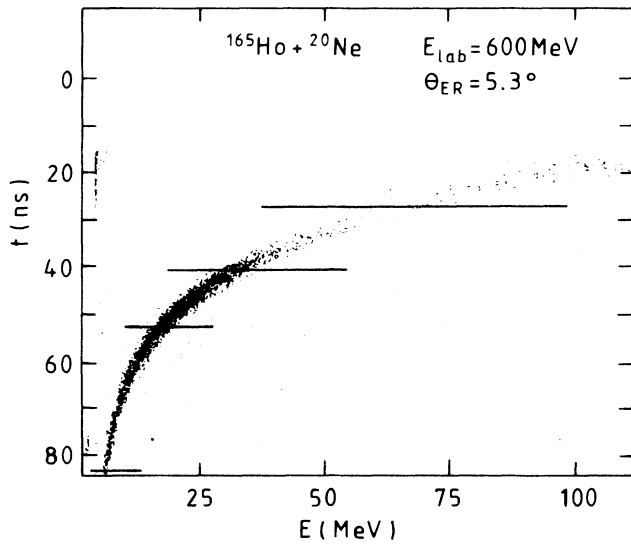


FIG. 1. Heavy-ion time of flight vs energy. Complete fusion would correspond to 45 MeV and 35 ns, taking into account energy loss in the target, ionization defect in the detector, and evaporation of 20 mass units. The straight lines indicate the three windows used to sort the neutron spectra.

metries introduced by the neutron recoil on the detected heavy fragment. The energy thresholds of the neutron detectors were set between 1.4 and 2.5 MeV. The efficiencies were calculated with a modified version of the Monte Carlo code of Cecil *et al.*⁵

A 2 mm thin plastic scintillator (NE102) was positioned in front of each neutron detector in order to detect any energetic charged particles which might reach the neutron detector and be detected with an efficiency of 100%, whereas a neutron of, e.g., 100 MeV would have a detection efficiency of only 5%. For detector no. 6 at 14° the scintillation-light resolution was good enough to

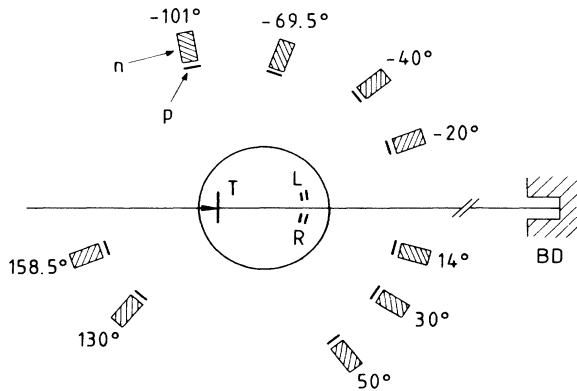


FIG. 2. Experimental setup: n and p stand for neutron detector and proton paddle, respectively, T denotes targets; L and R denote left and right ER detector; and BD denotes the beam dump, which was 5 m downstream from the target.

TABLE I. Neutron detector positions.

Angle (deg)	Path length (cm)	Detector no.
14.0	175.4	6
-20.0	175.7	4
30.0	175.9	5
-40.0	176.1	3
50.0	175.9	2
-69.5	143.6	1
-101.0	143.7	7
130.0	124.8	9
158.5	124.9	8

separate protons, deuterons, and tritons, making it possible to compare the neutron energy spectra with those of energetic hydrogen ions. The separation is shown in Fig. 3.

A velocity distribution of the heavy fragments with masses larger than 100 amu as measured at a TOF path length of 39 cm at 5.6° is shown in Fig. 4. As can be seen, the velocity distribution is very broad, ranging from full to 25% linear-momentum transfer (LMT). The low velocity cutoff is caused by an experimental threshold of the fragment detector. In order to discriminate between central and peripheral collisions, it is necessary to measure neutrons as a function of LMT. However, it is not necessary to make the velocity windows too narrow, since evaporation of light particles causes considerable smearing of the fragment velocities. We have chosen the velocity windows such that they match the FWHM of the velocity broadening of the evaporation process as calculated with the evaporation code JULIAN.⁶ This results in three velocity windows of 0.36–0.57, 0.57–0.73, and 0.73–

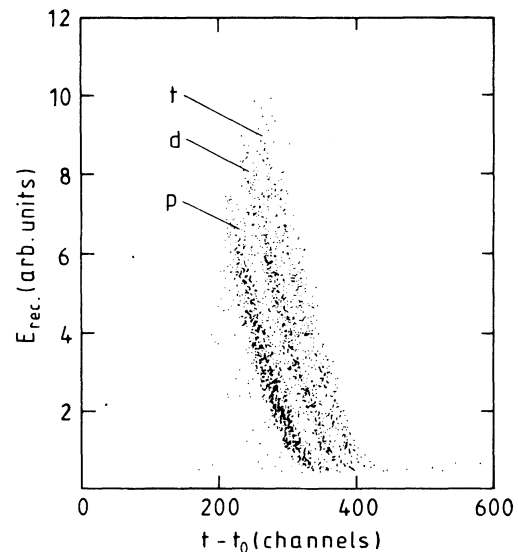


FIG. 3. Separation of hydrogen isotopes. E_{rec} is the light in the neutron detector and $t - t_0$ the time of flight.

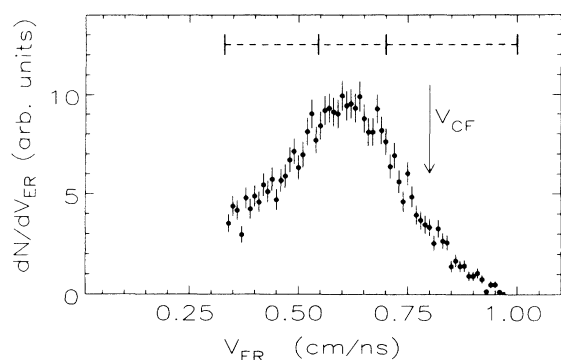


FIG. 4. Velocity distribution of evaporation residues in the laboratory system at 5.6; the vertical bars indicate the velocity cuts for which the coincident neutron spectra were measured. V_{CF} corresponds to the velocity of complete fusion taking into account the energy loss in the target.

1.00 cm/ns; the corresponding mean velocities (LMT) at $\theta_{lab}=5.3^\circ$ were 0.454 ± 0.005 cm/ns (52%), 0.620 ± 0.010 cm/ns (73%), and 0.775 ± 0.016 cm/ns (93%), respectively. These velocities are corrected for the plasma delay⁷ (about 2 ns) of the heavy fragments in the solid state detectors used and the energy loss in the target. The given errors for the mean velocities reflect the uncertainty of ± 1 ns for the TOF at a path length of 39 cm. The velocity of complete fusion corresponds to 0.829 cm/ns. In the figures the velocity distributions are not corrected for the energy loss in the target.

In order to obtain information on cross sections and relative probabilities for various reaction processes, in a separate experiment angular distributions of fission fragments (FF's) and ER's have been measured in a 1-m-diam scattering chamber. Two pairs of solid-state $\Delta E - \Delta E$ detector telescopes each with an aperture of 5 mm in diameter were mounted on two movable arms to the left and right of the beam. The telescopes of each pair had an angle of 2.2° relative to each other and were positioned at a distance of 39 cm from the target. The front detectors closest to the beam with a thickness of $20\ \mu\text{m}$ were intended for detection of ER's; all other detectors had a thickness of $120\ \mu\text{m}$. In order to reject elastic events and light particles, the same fast anticoincidence between front and back detector, as mentioned above, was applied. Two monitor detectors, consisting of a 0.5 mm thin NE102A plastic scintillator and a Hamamatsu R1288 photomultiplier tube, were placed at an in-plane angle of 0° and at out-of-plane angles of 17.2° and 6.4° . The systematic errors are estimated to be 10% for the absolute cross section and $\pm 0.1^\circ$ for the telescope angle positions. In Fig. 5 the quasielastic scattering cross section normalized to Rutherford scattering is shown. This normalization was employed for determining the absolute cross sections for fission fragments and evaporation residues. The solid line represents an optical-model calculation with parameters $V=40$ MeV, $r_{0V}=1.14$ fm, $a_V=0.7$ fm, $W=40$ MeV, $r_{0W}=1.2$ fm, and $a_W=0.5$ fm, yielding a reaction cross section of 3.4 ± 0.3 b.

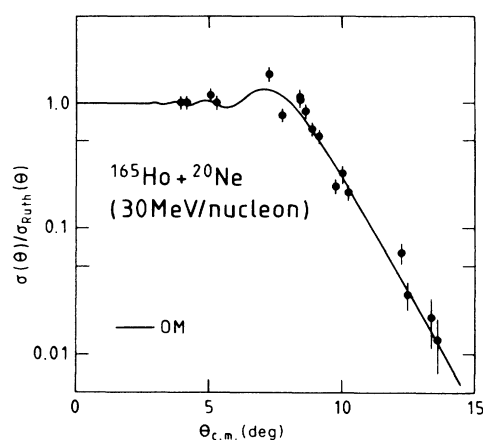


FIG. 5. Angular distribution of quasielastic scattering of ^{20}Ne on ^{165}Ho . The solid line is an optical-model (OM) fit. The OM parameters are given in the text.

To deduce the average linear momentum transferred to the fissioning system, the measurement of the folding angle between coincident fission fragments has been used extensively. An estimate of the average transferred linear momentum to the composite system can also be achieved by the comparison of fission-fragment differential cross sections at very forward and backward angles. The latter method is applicable for systems with relatively low center-of-mass velocities, in which case fragments also from asymmetric mass splits can be detected at backward angles. The effect of kinematic focusing is demonstrated in Fig. 6. For the transformation into the c.m. system, full linear-momentum transfer was assumed in the upper part of Fig. 6, whereas in the lower part only the transfer of ^{16}O with beam velocity (80% momentum transfer) was assumed. The good agreement between forward- and backward-angle cross sections in the lower part of Fig. 6 indicates that the average linear-momentum transfer for the fusion-fission process is 80%. Integration of the differential cross section yields 805 ± 80 mb for the fusion-fission reaction.

Particle emission from moving ER's causes a change in the original direction of flight. This recoil effect produces the final angular distribution of ER's and can be due to emission of evaporative or fast particles as well as to incomplete fusion events where linear momentum is exchanged between ER's and projectile-like fragments. Angular distributions of ER's for the three velocity bins mentioned above have been analyzed and are compared in Fig. 7. The narrowest angular distribution is obtained for ER's with the fastest velocity and the highest excitation energy. The curve in Fig. 7 has been calculated with the evaporation code JULIAN (Ref. 6) using the parameters to be deduced in Sec. III. For lower recoil velocities the angular distributions become broader and peak at angles of 4° – 6° , reflecting the focusing of the companion projectile-like fragment (with mass 6–10) towards the grazing angle. Integration of the experimental angular distribution yields 770 ± 80 , 540 ± 75 , and 240 ± 30 mb for

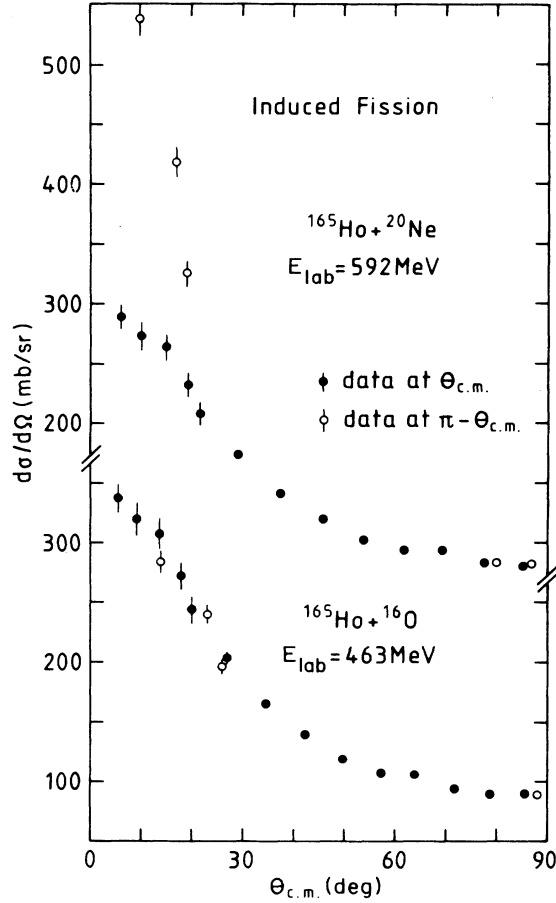


FIG. 6. Angular distribution of fission fragments. In the upper part of the figure the transformation into the c.m. system was performed by assuming that the c.m. velocity corresponds to that of complete fusion of $^{165}\text{Ho} + ^{20}\text{Ne}$, whereas in the lower part of the figure only fusion of mass 16 was assumed.

evaporation residues or target-like recoils in the three velocity bins of 0.36–0.57, 0.57±0.73, and 0.73±1.00 cm/ns, respectively. Summing up the cross sections for ER's or target-like recoils with velocities larger than 0.36 cm/ns and fission yields 2355 mb, corresponding to about 70% of the total reaction cross section.

The measured double differential neutron multiplicities as shown in Fig. 8 exhibit clearly two components, a low- and high-energy component, with essentially exponential slopes. Thus the spectra were fitted with two Maxwellian distributions transformed into the laboratory system:

$$\frac{d^2M_n}{dE_n d\Omega_n} = \sum_{i=1}^2 \frac{M_{ni} \sqrt{E_n}}{(2\pi T_i)^{3/2}} \times \exp \left[-\frac{E_n - 2\sqrt{\epsilon_i E_n} \cos \psi_i + \epsilon_i}{T_i} \right]. \quad (1)$$

The two sources are moving with different velocities corresponding to ϵ_i MeV/nucleon and emitting isotropically

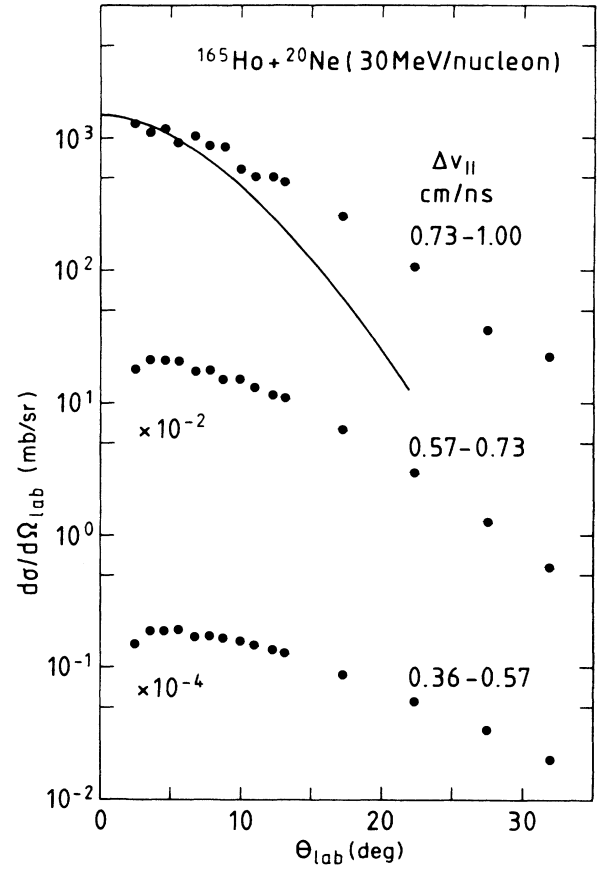


FIG. 7. Angular distribution of ER's for the three velocity bins of 0.36–0.57, 0.57–0.73, and 0.73–1.00 cm/ns, corresponding to LMT's of 52%, 73%, and 93%, respectively. For LMT=93% the angular distribution of ER's due to the evaporation of particles is given by the solid line as calculated with the evaporation code JULIAN.

neutrons with multiplicities M_{ni} and mean temperatures or exponential slopes T_i . The angle ψ_i is the angle between the direction of the source and the detected neutron and is assumed to be identical to the neutron angle θ_n since both sources are assumed to move to 0° . The distribution given by Eq. (1) was furthermore folded with the experimental time resolution assuming a Gaussian distribution with FWHM of 2.5 ns. However, the effect of the finite time resolution was small; the largest effect for 80 MeV neutrons at 14° is 12% of the neutron multiplicity for an energy distribution described by the parameters given in Table II. The variation of the deduced parameters for a time resolution of 0 or 2.5 ns was smaller than the given errors. The finite binning of the neutron energies were also taken into account.

The assumption that all heavy fragments are moving to 0° is certainly true for the PE component and for the evaporative component at the highest LMT, whereas for the smaller LMT the recoil angle is different from 0° , as can be inferred from Fig. 7. But the error made is small since the fragment velocities are small and thus the kinematic

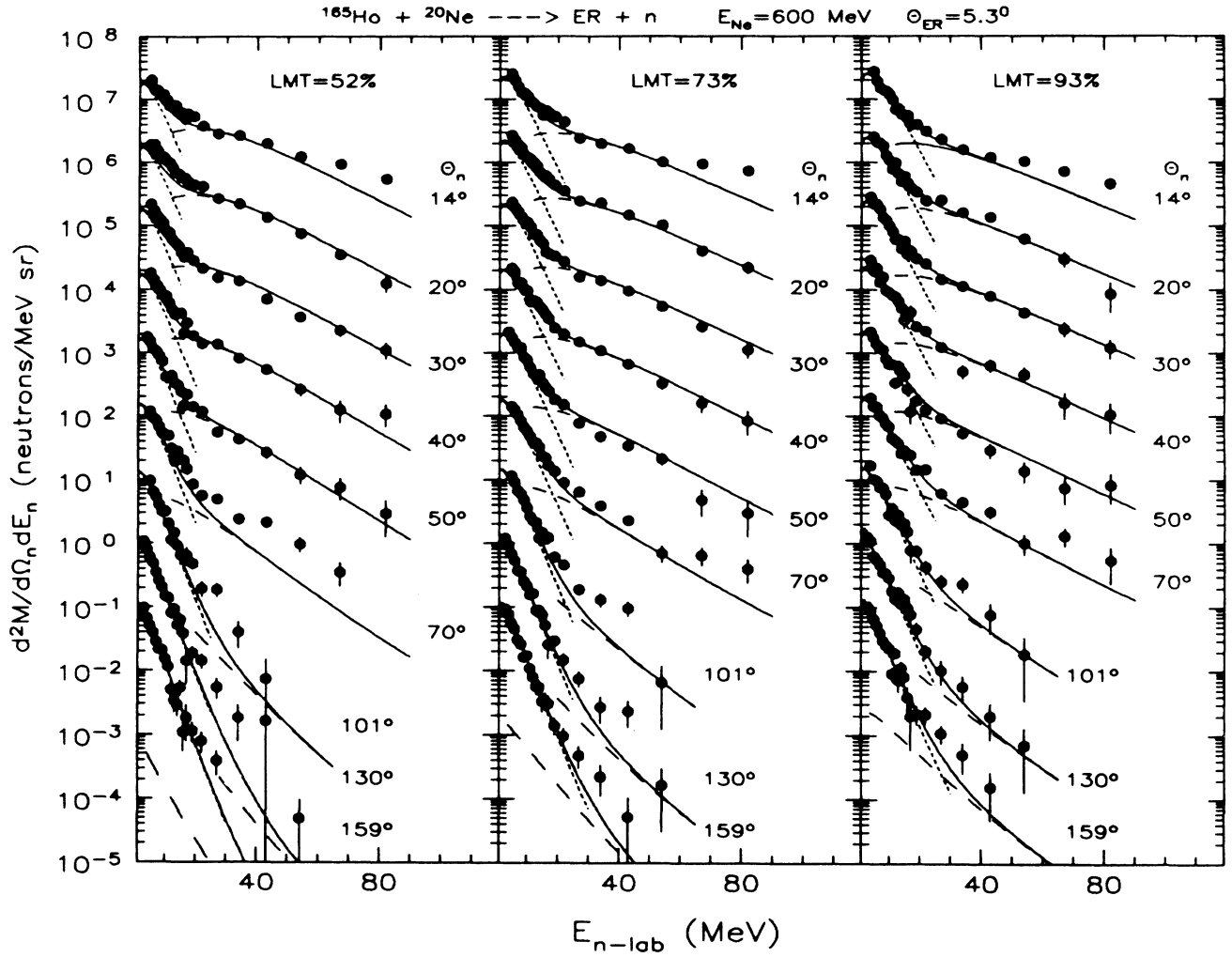


FIG. 8. Double differential neutron multiplicities in coincidence with evaporation residues with different linear-momentum transfer (LMT). The dotted and dashed lines correspond to the calculated distributions for the evaporative and preequilibrium component using the parameters given in Tables III and II, respectively; the solid line is the sum of both components. The curves and the data were multiplied with 10^k , where $k=0,1,2,3,\dots$, and 8 for $\theta_n=159^\circ, 130^\circ, 101^\circ, 70^\circ, \dots$, and 14° , respectively.

focusing is not changing much for a change in the mean relative angle of 5° – 10° .

The evaporative component was fitted for neutron energies between 6 and 14 MeV, whereas the preequilibrium component was fitted for neutron energies larger than 20 MeV. The low-energy end of 6 MeV was taken to be at

least 3 times larger than the neutron detection threshold in order to keep the uncertainty of the neutron detection efficiency smaller than 10%, which would correspond to a 30% variation of the threshold energy. The parameters of the fit and the corresponding χ^2 per point are given in Tables II and III. The source velocities of the evaporative

TABLE II. Parameters obtained by the least squares fit for the preequilibrium component. In the fit the finite time resolution of 2.5 ns was included as described in the text.

LMT (%)	M_{pe} (neutrons)	T_{pe} (MeV)	ϵ_{pe} (MeV/nucleon)	χ^2 ^a	v_{pe}/v_p (%)
52	2.5 ± 0.3	8.2 ± 1.0	12.5 ± 1.5	2.7	66 ± 4
73	3.1 ± 0.3	10.3 ± 1.2	9.8 ± 1.5	2.5	58 ± 4
93	2.9 ± 0.4	12.0 ± 1.8	6.8 ± 1.5	1.5	48 ± 4

^a χ^2 per point.

TABLE III. Parameters obtained by the least squares fit for the evaporative component. In the fit the finite time resolution was included as described in the text.

LMT (%)	M_{ev} neutrons	T_{ev} (MeV)	ϵ_{ev} (MeV/nucleon)	χ^2 ^a
52	11.6±0.6	3.13±0.10	0.106	1.2
73	14.4±0.8	3.39±0.10	0.197	1.5
93	17.0±1.0	3.74±0.14	0.308	1.2

^a χ^2 per point

component were taken from the measured velocities of the ER's corrected for the energy loss in the target. For the fit of the evaporative component only the measured spectra at the backward angles of $\theta_n = 101^\circ$, 130° , and 158.5° were used. The fits thus obtained are shown in Fig. 8.

The deduced neutron multiplicities and temperatures of the evaporative part are increasing with transferred linear momentum, which one would expect since increasingly more energy is dissipated. Further quantitative discussion will be given in Sec. III. In Fig. 9 the neutron multiplicity $dM/d\Omega(\theta_n)$ integrated between 5.5 and 17.5 MeV is given as a function of neutron detection angle. The dotted curves are calculated by using the parameters given in Table III for the evaporative component which were obtained by fitting *only* the three most backward angles. The contribution of the preequilibrium or high-energy component (Table II) at this energy region is shown by the dashed line. The solid line is the sum of both contributions. The observation that only for the highest LMT is the neutron multiplicity reproduced by the calculated curves indicates that low-energy neutrons are indeed evaporated isotropically by one source moving with the measured ER velocity into the beam direction. However, for smaller LMT there is clearly more yield at small angles than predicted by the above assumption. Our interpretation is that these excess neutrons are emitted from

projectile-like fragments which carry away part of the missing momentum, as already inferred from the broad sideways peaked angular distribution of ER's or, rather, target-like recoils. This means that the present experiment is not complete enough for small LMT to reconstruct the neutron energy spectra since the missing projectile-like fragments are not detected. For the highest LMT, on the other hand, the experiment is almost complete.

It should be pointed out that the temperatures given in Table III are only mean temperatures of the whole neutron cascade. The temperature of the first neutron according to Le Couteur and Lang⁸ is $\frac{12}{11}T_{ev}$. Thus the highest nuclear temperature measured in this experiment is then 4.1 ± 0.15 MeV. This is the temperature of the residual nucleus after the evaporation of the first neutron. If, however, charged particles are also evaporated, an additional correction for charged-particle emission is necessary, which will be discussed in Sec. III.

An interesting question of preequilibrium light-particle emission is whether these particles correlate with the impact parameter, which we assume to be smallest for the largest LMT. If the light-particle emission is dominated by nucleon-nucleon collisions, then one would expect that the apparent source velocity is smaller for more central collisions than for peripheral collisions, simply due to the fact that for central collisions the incoming nucleons have to traverse the whole target nucleus and thus have a larger probability to scatter and rescatter from target nucleons.^{9,10} We find that the deduced parameters of the preequilibrium component indicate that the source velocity is decreasing with increasing LMT, whereas the deduced slope parameter T_{pe} is increasing (see Fig. 11). However, since this results from the fit of the high-energy component of the spectra and is not immediately obvious by inspecting the spectra, it might be an artifact. Thus it is advantageous to inspect the angular distribution of high-energy neutrons, which is shown in Fig. 10. One observes that indeed the asymmetry as defined by the ratio

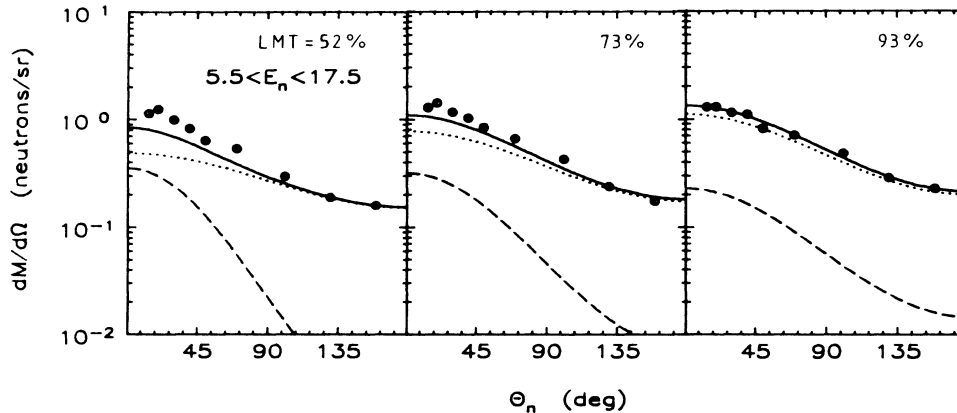


FIG. 9. Angular distribution of neutron multiplicity integrated over the neutron energy interval 5.5–17.5 MeV. The dotted and dashed lines correspond to the calculated contribution from the evaporative and preequilibrium component using the parameters given in Tables III and II, respectively; the solid line is the sum of both components.

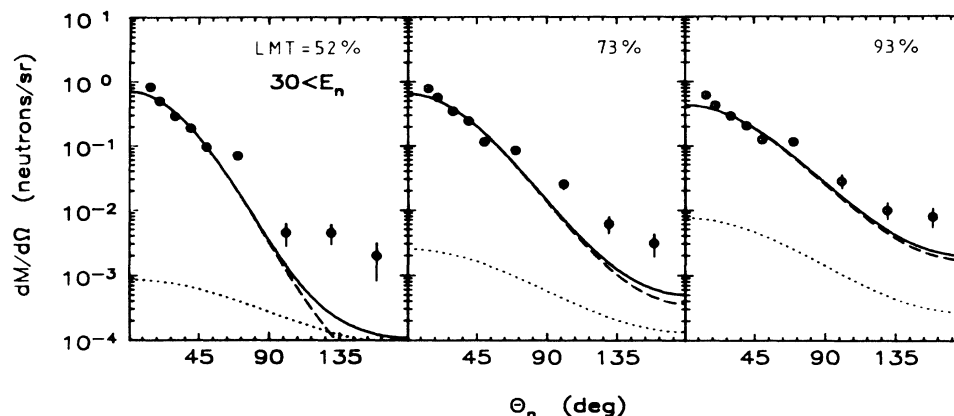


FIG. 10. Angular distribution of neutron multiplicity integrated over all neutron energies greater than 30 MeV. The curves have the same meaning as in Fig. 9.

of neutron multiplicity in the forward direction to that of the backward direction is smallest at the highest LMT of 93%. In particular, the ratio of

$$\frac{[dM/d\Omega(14^\circ) + dM/d\Omega(20^\circ)]}{[dM/d\Omega(130^\circ) + dM/d\Omega(159^\circ)]}$$

for LMT=52% is 3.6 ± 1.3 times larger than for

LMT=93%. Thus the data seem to indicate that for more central collisions the emission of preequilibrium neutrons is more isotropic. This also affects the quality of the fit, which is improving with increasing linear-momentum transfer, as can be seen from the given χ^2 in Table II.

Whether this is an indication of increasing nucleon re-scattering inside the target nucleus with decreasing impact parameter is, however, questionable. The observed increasing anisotropy of the PE component with decreasing LMT can be easily explained also by an increasing contribution of sequentially emitted neutrons from projectile-like fragments. As demonstrated in Fig. 11, a linear extrapolation of the source velocity v_{pe} to ER velocity $v_{er} \approx 0$ (that is, zero LMT) yields $\approx (92 \pm 10)\%$ of the beam velocity; thus for small LMT the source velocity just reflects this superposition. In order to really unfold the superposition from true preequilibrium emission during the interaction of the projectile and target nucleus and sequential emission, it would be necessary to measure neutrons in coincidence with target recoils and projectile-like fragments.

III. STATISTICAL MODEL, LEVEL DENSITY PARAMETER

Level density parameters have been deduced at low excitation energies of a few MeV by Dilg *et al.*¹¹ For applications of the statistical model, in particular evaporation calculations at high excitation energies of a few hundred MeV, it is usually simply assumed that a is independent of the excitation energy and equal to the value obtained at small energies. However, there is no theoretical reason that a should be independent of excitation energy. In fact, Dean and Mosel¹² and others¹³⁻¹⁵ have shown that a should decrease with increasing excitation energy. Dean and Mosel argue that due to the finiteness of the space of single particles a should decrease. From the above deduced mean temperatures of the evaporative component, we should, in principle, be able to infer the level density parameter a or the inverse level density parameter A/a , which is usually assumed to be a constant (A is the atomic

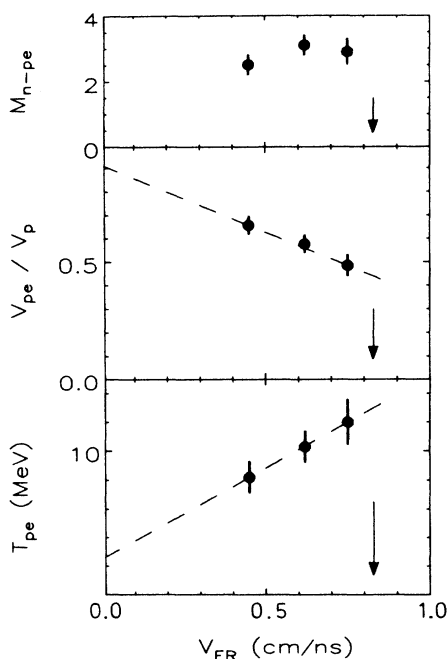


FIG. 11. The deduced parameters of the hot-moving source fit: temperature parameter T_{pe} , ratio of the source velocity to the beam velocity, v_{pe}/v_p , and the PE neutron multiplicity M_{n-pe} as a function of the ER velocity v_{ER} . The dashed line is drawn through the points and extrapolated to zero ER velocity. The arrows indicate full LMT.

mass number). The inverse level density parameter deduced by Dilg *et al.*¹¹ at low excitation energies in the mass region around $A \approx 180$ is 9.5 MeV. But, also, values between 7 and 14 MeV are used in the literature.

The basic relation⁸ we want to use to determine the level density parameter a is

$$E_{\text{th}}^* - B_n - 2T = aT^2, \quad (2)$$

where E_{th}^* , B_n and T is the thermal excitation energy, neutron binding energy, and temperature in the residual nucleus after emission of the first neutron. Although relation (2) is very convenient, it overestimates the nuclear temperature if charged particles are evaporated. In order to take this into account, we have performed evaporation calculations with the code JULIAN,⁶ which result in a decrease of the nuclear temperature by about 10–14% compared to Eq. (2). These calculations were done assuming evaporation of n, p, d, and α particles only, a triangular shaped spin distribution with a maximum spin of $65\hbar$, and ground state binding energies. The calculated temperature was determined from the first moment of the calculated center-of-mass neutron energy spectra and compared with the corresponding experimental value $1.5T_{\text{ev}}$ (Table III). This procedure was tested by fitting the calculated energy spectra for the same c.m. energy region and the same spectral shape as was done with the measured neutron spectra. Thus, evaporation calculations have been used throughout instead of the simple equation (2).

In the following we want to deduce the inverse level density parameter A/a by two methods, both of which exploit implicitly the above given relation, whereas E^* used in the evaporation calculations is obtained in two independent ways: (1) from the measured LMT taking into account the preequilibrium light particle emission, and (2) from the measured neutron multiplicity by means of an evaporation code. From the comparison of both methods, we can test our interpretation of the parameters given in Table II for the preequilibrium neutron emission.

In the massive transfer model it is assumed that a certain fraction of the projectile transfers its full linear momentum to the target, whereas the remaining part of the projectile acts only as spectator and continues with beam velocity v_p . With this assumption one obtains, for the mean excitation energy $\langle E^* \rangle$ of the thus partially fused system from its measured mean velocity $\langle v_{\text{ER}} \rangle$,

$$\langle E^* \rangle = m_T \epsilon_p \left[1 - \left(\frac{v_p}{c} \right)^2 \right]^{1/2} \frac{\langle v_{\text{ER}} \rangle}{v_p} + \langle Q_{\text{gg}} \rangle - \langle E_{\text{pe}} \rangle, \quad (3)$$

where m_T , ϵ_p , c and $\langle Q_{\text{gg}} \rangle$ are mass of the target, energy per nucleon of the projectile, speed of light, and ground state Q value of the incomplete fusion reaction. The square root in Eq. (3) is a correction for relativistic effects of about 3%.

The last term, $\langle E_{\text{pe}} \rangle$, in Eq. (3) is the mean energy carried away by preequilibrium light-particle emission *in excess* of the kinetic energy connected with the mean linear momentum parallel to the beam direction taken off by these particles. The latter is already taken into account by

the first term in Eq. (3). From the neutron spectra shown in Fig. 8, it is obvious that highly energetic neutrons are also emitted perpendicular to the beam direction. Thus it is not a question of whether one should use the last term in Eq. (3) or not, but rather how to calculate it. We employ the physical picture of a hot moving source in order to separate the mean kinetic energy $M_{\text{pe}} 1.5T_{\text{pe}}$ carried away isotropically by the PE neutrons from the kinetic energy of the ordered motion parallel to the beam with linear momentum $M_{\text{pe}} m_0 \sqrt{2\epsilon_{\text{pe}}}$, where m_0 stands for the nucleon mass. By comparing this linear momentum with the measured LMT of 52%, 73%, and 93%, we find that $M_{\text{pe}} m_0 \sqrt{2\epsilon_{\text{pe}}}$ makes up for about 17%, 32%, and 92% of the *missing* linear momentum (LM). From the comparison of the neutron and proton spectra measured at 14° for energies larger than 70 MeV, we find, however, that about half as many protons are emitted. Thus the missing LM is more than accounted for by preequilibrium light-particle emission for the highest LMT window of 93%. The latter finding is probably due to an overestimation of the PE multiplicity by assuming that the spectral shape for PE emission is also true for small neutron energies underneath the large evaporative component. For smaller LMT other processes are contributing, so that only a small fraction of the missing LM is found in PE nucleon emission. The actually used $\langle E_{\text{pe}} \rangle = M_{\text{pe}} 1.5T_{\text{pe}} - \delta$ was calculated by using only the neutron data given in Table II for LMT=93% and neglecting any PE emission of protons. The correction δ takes into account that in the first term of Eq. (3) it is assumed that 1.5 nucleons (for the highest LMT) do not fuse with the target, but leave the interaction zone with beam velocity, whereas experimentally twice as many (2.9) PE neutrons are emitted with half the beam velocity. Though the missing LM is the same, the missing excitation energy is not. The mean many body Q value used was that for the reaction $^{165}\text{Ho} + ^{20}\text{Ne} \rightarrow ^{182}\text{Ir} + 3n$. This results in $\langle E^* \rangle = 410$ MeV, and by employing the measured mean temperature T_{ev} from Table III, we obtain $A/a = 10.4 \pm 2$ MeV. The neutron multiplicity calculated with this level density parameter and excitation energy for the compound nucleus ^{182}Ir is 16.25 neutrons, which is already close to the measured value of 17.0 ± 1.0 . If, on the other hand, we set $\langle E_{\text{pe}} \rangle$ to zero, we obtain $\langle E^* \rangle = 454$ MeV and $A/a = 9.1$ MeV. The corresponding calculated neutron multiplicity is 18.6, which is larger than the measured value. Consequently, the true excitation energy must be smaller than 454 MeV. The deduced A/a values, by assuming $\langle E_{\text{pe}} \rangle = 0$, and the corresponding excitation energies, are given for all three LMT in columns 7 and 6 of Table IV, respectively.

So far, we have used only the mean temperature and velocity of the ER's, whereas in the second method we exploit only the measured multiplicity M_{ev} and temperature T_{ev} of evaporated neutrons to deduce the excitation energy and the level density parameter. In the statistical model the multiplicity of emitted light particles depends primarily on the excitation energy, but also on the level density parameter. Thus, by varying the excitation energy and level density parameter as the input of an evaporation code until the measured neutron multiplicity and tempera-

TABLE IV. Excitation energies and Q values.

v_{ER} (cm/ns)	$\langle E_{c.m.} \rangle^a$ (MeV)	m_t^b (u)	AZ_t	Q_{gg}^c (MeV)	$\langle E^* \rangle^d$ (MeV)	A/a^e (MeV)	$\langle E^* \rangle^f$ (MeV)	A/a^f (MeV)
0.454	293	10.4	${}^{10}\text{B}$	-61.7	231	11.8 ± 0.8	225 ± 20	12.1 ± 1.0
0.620	400	14.5	${}^{14}\text{N}$	-46.2	354	9.3 ± 0.6	310 ± 26	10.8 ± 0.8
0.775	500	18.5	${}^{18}\text{F}$	-45.6	454	9.1 ± 0.7	414 ± 40	10.2 ± 1.0

^a $\langle E_{c.m.} \rangle$ from $\langle v_{ER} \rangle$ using the first term in Eq. (3).

^b $m_t = m_T [v_{ER} / (v_p - v_{ER}) (1 - \beta_p^2)^{1/2}]$ transferred mass.

^c Q_{gg} corresponds to the assumed reactions ${}^{20}\text{Ne} + {}^{165}\text{Ho} \rightarrow {}^{175}\text{Hf} + n + p + 2\alpha$, ${}^{179}\text{W} + n + p + \alpha$, and ${}^{183}\text{Os} + n + p$.

^d $\langle E^* \rangle = \langle E_{c.m.} \rangle + Q_{gg}$.

^eUsing $\langle E^* \rangle$ (see footnote d) and T_{ev} .

^fUsing M_{ev} and T_{ev} only.

ture are reproduced, we obtain, for the highest velocity bin, $\langle E^* \rangle = 414 \pm 40$ MeV and $A/a = 10.2 \pm 1$ MeV. The excitation energies and level density parameters deduced with this method are given for all LMT in columns 8 and 9 of Table IV, showing that the deduced excitation energies (column 8) are all systematically smaller than the corresponding excitation energies deduced only from the LMT (column 6), neglecting $\langle E_{pe} \rangle$. This demonstrates the necessity of the term $\langle E_{pe} \rangle$ in Eq. (3).

In a preliminary report¹⁶ we used the first method and obtained $A/a = 10.5 \pm 1.5$ by employing Eq. (2) only, thus neglecting the effect of charged particles in the evaporation chain. Furthermore, there was still an error in the velocity of the ER by not taking into account the plasma delay in the solid state detectors, resulting in too small a LMT. Both effects canceled each other, so the result was almost the same as the present one.

The results for the inverse level density parameter are given for all velocity bins in Table IV (column 9). The deduced values agree within the errors for the two highest velocity bins, whereas for the smallest velocity A/a is considerably larger. The reason for this latter finding is not completely understood, but it might be caused by the superposition of many different processes, as can be seen from the angular distribution of the evaporated neutrons as shown in Fig. 9. Another possibility might be that the bin width for the smallest LMT is too narrow, so that higher LMT and thus also higher excitation energies are strongly-contributing. This is corroborated by the sideways peaked angular distribution of ER's or target-like recoils, as shown in Fig. 7 and discussed in Sec. II. These higher excitation energies tend to increase the measured temperature and consequently increase the inverse level density parameter. This argument points to the fact that the most reliable A/a value is that deduced for the highest LMT. Thus we use only the LMT's of 73% and 93% to determine the level density parameter at excitation energies of ≈ 300 – 400 MeV to be $a = A / (10.5 \pm 1) \text{ MeV}^{-1}$.

The level density parameter deduced by Dilg *et al.*¹¹ for the mass region $A \approx 180$ is $A/9.5$, which agrees with the above given value for a ; thus the present results do not indicate that the level density parameter a is decreasing with excitation energy. Very recently, Nebbia *et al.*¹⁷ have determined the level density parameter from measured α spectra, finding a decrease of a from $A/8$ to

$A/13$ for excitation energies from 100 to 400 MeV for compound nuclei with $A \approx 160$. More precisely, Nebbia *et al.* obtained, for temperatures of 3.7 and 4.8 MeV, inverse level density parameters of $A/a = 10.6 \pm 1$ and 12.2 ± 1 MeV, respectively, which agree within the error bars with the present value of 10.5 ± 1 at a temperature of about 4.8 MeV. The present result depends on approximations made in the evaporation code; in particular, it is assumed that the transmission coefficients can be calculated with the shapes of cold nuclei. To test this assumption we have increased the radius parameters in the optical model potentials by 10%. The effect on the mean neutron temperature is 1%, whereas the neutron multiplicity is decreased by about 8%, which would increase the level density parameter also by about 10% in order to obtain the same mean neutron multiplicity and temperature as was obtained with the standard radius parameters. Furthermore, the effect of biasing the neutron multiplicity by measuring the neutrons in coincidence with evaporation residues at $5.3^\circ \pm 0.5^\circ$ was investigated by requiring in the evaporation calculations that the ER's at the end of the evaporation chain move into the same angular window as in the experiment. The calculated mean neutron multiplicities and temperatures with and without this requirement are the same within 0.5%, which is the accuracy of the Monte Carlo calculation.

The level density parameter $A/10.5$ was used to calculate the multiplicity and the mean temperature of neutrons as a function of the ER velocity. The excitation energies have been calculated from the LMT and are given in column 6 of Table IV. The results are compared with the experimental values in Fig. 12. Finally, the deduced level density parameter and excitation energy can be used to determine the maximum thermodynamical temperature reached in the fusion-like reaction $\text{Ho} + 600 \text{ MeV Ne}$ at a LMT of about 93%. Using the relation $T = [(\langle E^* \rangle - E_{rot})/a]^{1/2}$ with 14 MeV for the rotational energy E_{rot} , we calculate the nuclear temperature of the primary fragments to be 4.8 MeV.

IV. COMPARISON WITH PREEQUILIBRIUM MODELS

Preequilibrium neutron spectra in coincidence with ER's of the reaction $\text{Ho} + \text{Ne}$ at lower bombarding energies have been used to test models of preequilibrium

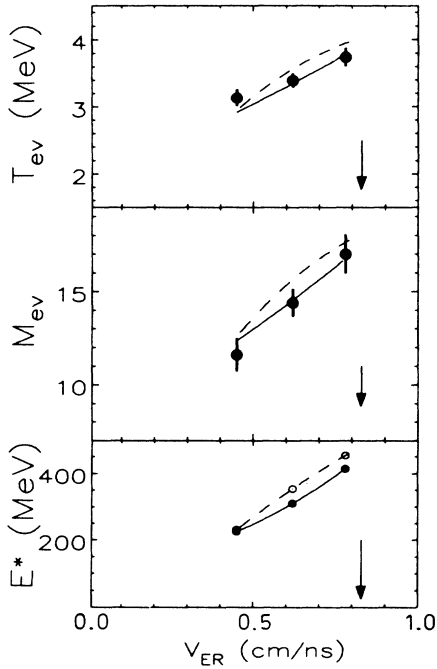


FIG. 12. Multiplicity M_{ev} and mean temperature T_{ev} of evaporated neutrons as a function of the ER velocity v_{ER} . The arrows indicate full LMT. The experimental determined points are compared with an evaporation calculation employing a level density parameter of $a = A/10.5 \text{ MeV}^{-1}$ and excitation energies E^* given in the lower part of the figure which were taken from columns 6 (dashed line) and 8 (solid line) of Table IV.

light-particle emission^{3,4,18} or to determine free parameters of such models.¹⁹ The comparison⁴ with the Fermi jet model of Bondorf *et al.*²⁰ has shown that this model is not able to describe the highly energetic neutrons emitted perpendicular to the beam axis. This was ascribed⁴ to the neglect of rescattering^{4,10} of highly energetic nucleons inside the composite system. On the other hand, Leray *et al.*¹⁸ found reasonable agreement with the neutron data³ also at angles close to 70° with an improved treatment of the Fermi jet mechanism, the improvement concerning, in particular, the window geometry. However, the rescattering effect was not taken into account, so that this agreement was a surprise. It turned out, however, that this was due²¹ to an error in the code of Leray *et al.*¹⁸ In Fig. 13 the neutron energy spectra of the present work summed over all LMT's are compared with the corrected code of Leray *et al.*¹⁸ It should be emphasized that the calculated multiplicities were not normalized to the data, so that the reasonable agreement at small angles is impressive. On the other hand, the figure clearly shows the inability of this model to describe the neutron spectra at angles close to 90° . However, the better treatment of the window geometry has improved the agreement at large backward angles greater than 101° . The disagreement at neutron energies around 30 MeV at forward angles might be due to sequential emission from projectile-like frag-

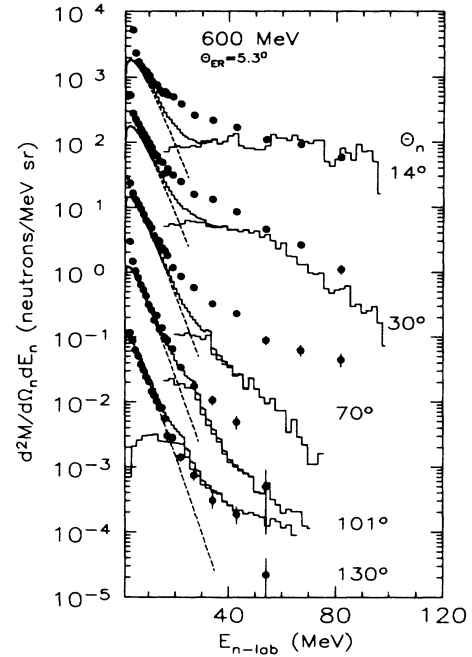


FIG. 13. Comparison of the double differential neutron multiplicity integrated over all LMT with results of the Fermi jet model of Leray *et al.* (Ref. 18). The dashed line corresponds to the evaporative component as obtained with the least squares fit. The sum of both components is also shown. The spectra were multiplied with 10^k for $\theta_n = 130^\circ, 101^\circ, 70^\circ, 30^\circ,$ and 14° , with $k = 0, 1, 2, 3,$ and 4 , respectively.

ments as discussed above for even smaller neutron energies. In any case the calculated spectra show a spectral shape completely different from that used in the hot-moving-source parametrization, indicating that it might be erroneous to use these spectral shapes to extrapolate the PE component underneath the evaporative component.

A model that includes all scattering and rescattering effects of nucleons inside a mean field is the model based on the Boltzmann-Uehling-Uhlenbeck (BUU) equation, which was treated by Aichelin⁹ and Grégoire *et al.*²² This model should also be able to predict the difference in PE spectra of neutrons and protons. By comparing the measured neutron and proton spectra at 14° and energies between 70 and 100 MeV, we find for linear-momentum transfers of 52%, 73%, and 93% that the multiplicity of neutrons is larger by a factor of $1.4 \pm 0.2, 1.7 \pm 0.3,$ and 2.4 ± 0.3 , respectively. The relative ratios of deuterons and tritons are given in Table V. Qualitatively, one does expect the emission of high-energy neutrons to be more likely since the n-p cross section at energies of about 100 MeV is 3 times larger than the p-p or n-n cross section. This implies a smaller absorption of neutrons in the neutron-rich target nucleus. Similar neutron/proton ratios were found also for 400 MeV/nucleon Ne + U, which were partly explained by Stevenson²³ by employing the coalescence model. It would be very interesting to com-

TABLE V. Ratio of multiplicities of neutrons to protons, protons to deuterons, and protons to tritons at 14° and energies between 70 and 100, 100 and 130, and 110 and 130 MeV, respectively.

LMT	n/p	p/d	p/t
52%	1.43 ± 0.2	1.13 ± 0.1	1.13 ± 0.1
73%	1.71 ± 0.3	1.37 ± 0.1	1.68 ± 0.1
93%	2.37 ± 0.2	1.41 ± 0.1	2.04 ± 0.2

pare the present data to the BUU model. However, it is important to treat neutrons and protons separately by using realistic nucleon-nucleon cross sections.

V. CONCLUSIONS

We have shown that the probability to transfer a linear momentum of 93% of its maximum value in the fusion-like reaction of $^{165}\text{Ho} + 600 \text{ MeV } ^{20}\text{Ne}$ is about 7% of the total reaction cross section. The temperature reached in this process is 4.8 MeV. That is, we find compound nuclei which are still dynamically stable and deexcite via the evaporation of light particles. The level density parameter $a = A/(10.5 \pm 1.0) \text{ MeV}^{-1}$ of these hot nuclei with $A \approx 180$ is very similar to that found for cold nuclei, while other experiments¹⁷ as well as theoretical investigations have found that the level density parameter is decreasing for nuclear temperatures between 4 and 5 MeV. Although in the present investigation the decrease of the level density parameter could not be shown, the deduced absolute values agree within the error bars with those of Nebbia *et al.*¹⁷ There is additional work needed before one can draw final conclusions since there are many assumptions and thus also possible uncertainties going into the deduction of the level density parameter. For instance, the fluctuations of excitation energies of the fused system can sensitively influence the measured temperatures. But, also the assumption of the sequence of light particles in the evaporation chain affects the final results. We have assumed that this decay chain is given essentially by the spin dependent level densities and the transmission coefficients of spherical nuclei and the respective ground state binding energies. Kasagi *et al.*²⁴ have pointed out that the effective radius parameter r_0 , which determines the spin cutoff factor in the level densities also affects the neutron spectra, however, only at small neutron energies, so that this can be neglected in our case.

An interesting by-product of the determination of the level density parameter is the interpretation of the parameters of the preequilibrium neutron spectra, as obtained

from a hot-moving-source fit. By comparing the results of both methods to determine the excitation energy and by reconstructing the missing linear momentum for the highest LMT, we find indications that the absolute value of the preequilibrium neutron multiplicity of 2.9 is too large. One should keep in mind that this parameter relies heavily on the assumed spectral shape of the preequilibrium neutron spectra which is different from the spectral shape, as, e.g., calculated by the Fermi jet model. If one integrates all preequilibrium neutrons with energies larger than 25 MeV, one obtains a multiplicity of only 1.1. Furthermore, the different methods to determine the equilibrium excitation energy of the compound nuclei have shown that an equation like Eq. (3) has to be used with the last term $\langle E_{pe} \rangle$ different from zero.

No drastic difference or discontinuities are observed for the neutron energy spectra compared to those at bombarding energies below the mean Fermi energy. However, it is no more possible to achieve a reasonably good fit with a hot-moving-source parametrization for all ER velocities. This is probably trivial since at these high bombarding energies many different processes are producing heavy fragments at small angles ranging from target-like recoils to evaporation residues. However, the preequilibrium neutron multiplicity is constant for all LMT between 52% and 93%, so that at small LMT an increasing fraction of the missing linear momentum must be carried away by heavier fragments in addition to PE nucleons. We find that the forward-to-backward asymmetry of the preequilibrium neutron yield is smallest for the highest LMT, pointing to an increase of rescattering effects and/or decrease of sequential emission from projectile-like fragments for the more central collisions.

A comparison with the Fermi jet model of Leray *et al.*¹⁸ shows agreement only at small and large angles, whereas no agreement is found at angles close to 90° , similarly to the findings of previous investigations.^{3,4} However, it would be interesting to compare the present results with the BUU equation which treats simultaneously effects from the mean field and from nucleon-nucleon collisions. In particular, it would be interesting to compare preequilibrium neutron and proton spectra. This might be a good experimental test for preequilibrium mechanisms since the ratio of neutrons to protons should reflect the neutron to proton ratio of the location where they were produced and of the nucleus through which they have passed.

We are grateful to S. Leray for performing the Fermi jet calculations and to the SARA staff for providing excellent beams.

*Permanent address: Deutsches Elektronen-Synchrotron, Hamburg, Federal Republic of Germany.

¹T. C. Awes, G. Poggi, C. K. Gelbke, B. B. Back, B. G. Glagola, H. Breuer, and V. E. Viola, *Phys. Rev. C* **24**, 89 (1981).

²A. Gavron, J. R. Beene, B. Cheynis, R. L. Ferguson, F. E.

Obenshain, F. Plasil, G. R. Young, G. A. Pettitt, and C. F. Maguire, *Phys. Rev. C* **27**, 450 (1983); A. Gavron, J. R. Beene, R. L. Ferguson, F. E. Obenshain, F. Plasil, G. R. Young, G. A. Pettitt, K. Geoffroy-Young, M. Jääskeläinen, D. G. Sarantites, and C. F. Maguire, *ibid.* **24**, 2048 (1981).

- ³E. Holub, D. Hilscher, G. Ingold, U. Jahnke, H. Orf, and H. Rossner, *Phys. Rev. C* **28**, 252 (1983).
- ⁴E. Holub, D. Hilscher, G. Ingold, U. Jahnke, H. Orf, H. Rossner, W. P. Zank, W. U. Schröder, H. Gemmeke, K. Keller, L. Lassen, and W. Lücking, *Phys. Rev. C* **33**, 143 (1986).
- ⁵R. A. Cecil, B. D. Anderson, and R. Madey, *Nucl. Instrum. Methods* **161**, 439 (1979).
- ⁶M. Hillman and Y. Eyal, JULIAN (unpublished), modified by H. Rossner.
- ⁷W. Bohne, W. Galster, K. Grabisch, and H. Morgenstern, *Nucl. Instrum. Methods A* **240**, 145 (1985).
- ⁸K. J. Le Couteur and D. W. Lang, *Nucl. Phys.* **13**, 32 (1959).
- ⁹J. Aichelin, *Phys. Rev. C* **33**, 537 (1986).
- ¹⁰W. Cassing, in *Proceedings of the Workshop on Coincident Particle Emission from Continuum States in Nuclei*, Bad Honnef, 1984, edited by H. Machner and P. Jahn (World-Scientific, Singapore, 1984), p. 340.
- ¹¹W. Dilg, W. Schantl, H. Vonach, and M. Uhl, *Nucl. Phys.* **A217**, 269 (1973).
- ¹²D. R. Dean and U. Mosel, *Z. Phys.* **A322**, 647 (1985).
- ¹³P. Bonche, S. Levit, and D. Vautherin, *Nucl. Phys.* **A436**, 265 (1985).
- ¹⁴R. W. Hasse and P. Schuck, *Phys. Lett.* **179B**, 313 (1986).
- ¹⁵A. Lejeune, P. Grangé, M. Martzolff, and J. Cugnon, *Nucl. Phys.* **A453**, 189 (1986).
- ¹⁶D. Hilscher, H. Rossner, A. Gamp, U. Jahnke, A. Giorni, C. Morand, A. Dauchy, P. Stassi, B. Cheynis, P. Chambon, D. Drain, C. Pastor, and G. Pettit, in *Proceedings of the International Conference on Heavy Ion Nuclear Collisions in the Fermi Energy Domain*, Caen, 1986 [*J. Phys. (Paris) Colloq.* **47**, C4-381 (1986)].
- ¹⁷G. Nebbia, K. Hagel, D. Fabris, Z. Majka, J. B. Natowitz, R. P. Schmitt, B. Sterling, G. Mouchati, G. Berkowitz, K. Strozewski, G. Viesti, P. L. Gonthier, B. Wilkins, M. N. Namboodiri, and H. Ho, *Physics Lett.* **176B**, 20 (1986).
- ¹⁸S. Leray, G. La Rana, C. Ngô, M. Barranco, M. Pi, and X. Viñas, *Z. Phys. A* **320**, 383 (1985).
- ¹⁹M. Blann, *Phys. Rev. C* **31**, 1245 (1985).
- ²⁰J. P. Bondorf, J. N. De, G. Fáí, A. O. T. Karvinen, B. Jakobsson, and J. Randrup, *Nucl. Phys.* **A333**, 285 (1980).
- ²¹S. Leray, private communication.
- ²²C. Grégoire, B. Remaud, F. Scheuter, and F. Sebille, *Nucl. Phys.* **A436**, 365 (1985).
- ²³J. D. Stevenson, *Phys. Rev. Lett.* **45**, 1773 (1980).
- ²⁴J. Kasagi, B. Remington, A. Galonsky, F. Haas, J. J. Kolata, L. Satkowiak, M. Xapsos, R. Racca, and F. W. Prosser, *Phys. Rev. C* **31**, 858 (1985).